Available online at www.sciencedirect.com

ScienceDirect

Journal of Catalysis 251 (2007) 131–144

JOURNAL OF CATALYSIS

www.elsevier.com/locate/jcat

A comparative study of the photocatalytic oxidation of propane on anatase, rutile, and mixed-phase anatase–rutile TiO_2 nanoparticles: Role of surface intermediates

T. van der Meulen, A. Mattson, L. Österlund [*,1]

Department of Environment and Protection, FOI, SE-901 82 Umeå, Sweden

Received 2 April 2007; revised 30 May 2007; accepted 4 July 2007

Abstract

The photocatalytic oxidation of propane was investigated by simultaneous in situ diffuse reflectance Fourier transform infrared spectroscopy (DRIFTS) and quadrupole mass spectrometry (QMS) on anatase, rutile, and mixed anatase–rutile TiO_2 nanoparticles prepared by hydrothermal treatments of microemulsions. The mixed anatase–rutile sample was compared with a commercial sample (Degussa P25) with similar anatase to rutile mol% ratio. The measured carbon mass balance for the different TiO_2 materials reveals that the total oxidation rate (propane → CO_2) over the first 25-min illumination period is highest for samples containing large anatase nanoparticles and that mixed anatase–rutile nanoparticles are superior to single-phase anatase nanoparticles. These findings are correlated with the main intermediate surface species observed on the different nanoparticle systems by DRIFTS. In particular, η^1-acetone and bridging bidentate formate (μ-formate) is detected. On both anatase and rutile, μ-formate is the final hydrocarbon surface species. Further oxidation yields bicarbonate, carbonate, CO_2, and H_2O. On all TiO_2 samples, the concentration of surface intermediates is found to be proportional to the accumulated carbon concentration, as deduced from the gas-phase carbon mass balance measurements. This shows that the rate-determining step is the oxidation of strongly bound surface intermediates. Furthermore, it is found that the rate-determining step is structure-sensitive. On anatase, photo-oxidation of acetone limits the total oxidation, whereas on rutile, formate does so. The latter is attributed to a combination of thermal dissociation of acetone on defect sites, which aids acetone oxidation, and the strong bonding of μ-formate to the (110) surface facets on rutile. A synergetic effect between anatase and rutile particles is observed, where the measured photo-oxidation rate from either QMS or DRIFT exceeds that for the individual constituent particles.

Keywords: Photocatalysis; Nanoparticles; TiO_2; Anatase; Rutile; Propane; Surface intermediates; Formate; Fourier transform infrared spectroscopy; Mass spectrometry

1. Introduction

Titanium dioxide photocatalysis is an environmentally acceptable method for air and water cleaning that has received considerable attention during the past 10–15 years [1–5]. There are, however, a number of questions in the area of gas–solid photocatalysis that must be solved if commercial devices based on semiconductors are to have a future as enduring air purification systems. In particular, in the case of air cleaning, dry photo-oxidation of organics has been shown to lead to a substantial decline in the reaction rate on TiO_2 nanoparticles during the initial reaction time. However, the nature of this deactivation is not known in detail [4,6,7], and there is a large spread in reported data that which appears to depend on the particular structure, size, and morphology of the different TiO_2 photocatalysts. One important aspect of gas–solid photo-oxidation over metal oxides is the formation of strongly bonded partial oxidation products on the surface, which can block or even irreversibly react with the oxide (under mild reaction conditions). It has been known since the 1960s that carbonate–carboxylate–

---

[*] Corresponding author. Fax: +46 90 106802.
E-mail address: lars.osterlund@foi.se (L. Österlund).

[1] Postal address: FOI NBC Defence, Cementv. 20, SE-901 82 Umeå, Sweden.

doi:10.1016/j.jcat.2007.07.002

formate (R–COO$^-$) species form on the surfaces of metal oxides on reaction with hydrocarbons [8,9]. Due to the strong bonding of these species to oxides such as TiO_2, it was even thought that they irreversibly reacted with the oxide and obstructed the catalytic action. However, it has been established, primarily by infrared spectroscopy, that R–COO$^-$ species are key intermediates in oxidation reactions, which, after interaction with O_2 (and O_2-derived species), decompose into CO_2 and H_2O or CO and H_2 depending on catalyst and reaction conditions [8–10]. The decomposition of R–COO$^-$ intermediates is known to be rate-determining in many cases [10,11]. However, the possibility of polymerization reactions or condensation reactions at high reactant concentrations may complicate the situation, with branching of the oxidation reaction leading to both complete oxidation and polyoxyhydrocarbon formation on the surface.

Alkanes are relevant model systems, because they occur both as pollutants (e.g., liquid petroleum gases) and as functional groups in a large class of organics. The oxidation of hydrocarbons on metal oxide catalysts has been studied extensively, and spectroscopic studies of reaction intermediates have been reviewed recently [10]. The photo-oxidation of alkanes was first studied systematically by Teichner et al. in the early 1970s [12–14]. Although these and many other studies [15] were conducted with high alkane concentrations, with interest directed toward partial oxidation, their main results are also valid for the photodegradation of trace amounts of hydrocarbons [4]. It is known that photocatalytic oxidation (PCO) of alkanes on TiO_2 proceeds via alcohol formation, and thus many of the reaction steps are expected to be analogous to those for the corresponding alcohols. Thus acetone is a common partial oxidation product in the PCO of C_3 hydrocarbon molecules and C_3 alcohols. Acetone is known to be stable and reacts further only under strongly oxidizing conditions (by C_α–C_β bond cleavage and methyl abstraction [16,17]). The selectivity for aldehydes is generally found to be lower. This is not surprising, considering that aldehydes are reducing and readily oxidized to carboxylic acid. Considering the protolysis of carboxylic acids to their corresponding ions (e.g., acetic acid to acetate or formic acid to formate), which are known to form strong complexes with transition metal cations [18], it is easy to understand why, for example, acetate and formate species are commonly observed on metal oxides such as TiO_2 (with concomitant hydroxylation of the surface) [10,19,20]. Considering this, there have been surprisingly few studies aimed at elucidating the elementary photoreaction steps of gas-phase carboxylic acids and aldehydes on different semiconductor nanoparticle systems [1,11,21,22]. In contrast, adsorption and thermal reactions of small carboxylate, and formic acid in particular, on both single-crystal [primarily rutile $TiO_2(110)$] [20,23–28] and TiO_2 nanoparticles have been studied extensively (see, e.g., [4,9,29,30] and references therein).

The present study is an extension of our previous work on the PCO of propane on anatase [7]. We provide detailed spectroscopic data of surface intermediates by in situ FTIR and correlate this to both online mass spectrometry data acquired simultaneously and to the surface structure of the different TiO_2 polymorphs, including mixed-phase TiO_2 containing both anatase and rutile and commercially available P25 (from Degussa), which has been used extensively in photocatalysis studies.

2. Experimental

2.1. Catalyst materials

Powders of aggregated TiO_2 nanoparticles were prepared by hydrothermal treatment of microemulsions as described elsewhere [31,32]. Anatase and rutile polymorphs prepared in a similar manner can be synthesized by this method, which facilitates comparison of the photocatalytic reactivity between different photocatalysts. In particular, we have shown that residuals from the surfactants (Triton X 100) and acids (HNO_3) used in the synthesis can be effectively removed by simple calcination of the final materials. Degussa P25 was used as a reference powder (two different batches). A powder was also synthesized to mimic the mixed-crystal structure of Degussa P25. The synthesized mixed oxide had a composition similar to that of Degussa P25, consisting of a mixture of anatase (≈80 at%) and rutile particles (≈20 at%). Table 1 shows the physical properties of the TiO_2 samples [31–33]. The specific area and pore size distribution were determined by the BET and BJH methods, respectively (using a Micromeritics ASAP 2010); the particle size and structure were determined by transmission electron microscopy (TEM), using a JEOL 1200 EX II; and X-ray diffraction (XRD) was performed using a Siemens D5000 diffractometer. The optical absorption edge was determined from UV–vis absorbance measurements using an integrating sphere accessory (Labsphere DRA-CA5500). The particle size in our anatase–rutile sample refers to the anatase phase; it was not possible to resolve the small rutile contribution by either TEM or XRD due to the weak signal. Table 1 shows that the mixed-phase anatase–rutile sample obtained in our synthesis consists of smaller particles and has a higher BET area than Degussa P25. The Degussa P25 samples contain the largest anatase particles in the present study (≈30 nm).

2.2. In situ reactivity measurements

Photocatalytic degradation experiments were done in a custom-modified reaction cell (Praying Mantis/HTHP, Harrick), which allowed simultaneous FTIR spectroscopy, irradiation of the TiO_2 catalyst by a UV source (300-W Xe arc lamp; Oriel), and online mass spectrometry detection of the composition of the reaction gas by quadrupole mass spectrometry (QMS), using a Pfeiffer QMG 422. Thus, true in situ experiments with simultaneous detection of gas-phase reactants and products (with QMS), as well as surface species (with FTIR) is accomplished. The reaction cell was mounted in a Bruker IFS-66v/S FTIR spectrometer equipped with a broadband MCT detector and connected to a home-built gas handling system consisting of a set of mass flow controllers (Bronkhorst).

The experiments were done in the flow mode, with the reaction gas (500 ppm propane, purity >99.998 vol%, AGA) was flowing over the powder catalyst bed in a carrier gas of synthetic air (20% O_2/N_2). The propane concentration was kept fixed at 500 ppm throughout the experiments. Control experiments with reactive adsorption of CO_2 (1% purity >99.99%, AGA) with water (deionized 18.2 MΩ) and deuterium (>99.96%, CIL) were done by passing the CO_2 gas through a liquid reservoir in a home-built humidifier held at constant temperature (284 ± 0.2 K). Formic acid (purity >98%, Merck) adsorption experiments were done by passing the synthetic feed gas through a home-built gas mixer [17]. A small fraction of the effluent gas stream from the reaction cell was continuously injected into a narrow nonactivated silica capillary colon (∼0.5 m long) placed directly above the TiO_2 sample bed, and fed into the QMS device through a directed gas inlet to optimize the gas stream over the ionization volume of the QMS cross-beam ion source [34]. The gas concentration detected in this manner represents the gas bulk (not influenced by concentration gradients above the sample). The temperature of the reaction cell sample cup was held at room temperature (293 K) during the experiments and controlled with a PID regulator. Before each experiment, the sample was heated in synthetic air at 723 K for 20 min and cooled in the same gas mixture. This procedure removed all organics from the TiO_2 surface as determined from the DRIFTS spectra. In particular, the brownish color that TiO_2 attains after prolonged UV illumination in a dry hydrocarbon reaction mixture is removed, and the powder appears white [7].

2.3. DRIFTS

FTIR spectra of powder samples were acquired in the diffuse reflectance mode with 2 cm^{-1} resolution and recorded in units of $\log(1/R)$ as a function of time with a time separation of 30–50 s between each measurement. Independent measurements showed no significant difference regardless of whether Kubelka–Munk or $\log(1/R)$ absorbance units were used. The main reason for choosing the $\log(1/R)$ representation is that decreasing (negative) bands can be readily distinguished from increasing band intensities (see Fig. 5 below). Each spectrum was averaged over 200 co-added scans. Before the analysis, the spectra were smoothed using a Savitzky–Golay algorithm with a 9-point window and were baseline-corrected. To better accentuate the photon-induced DRIFTS peaks in the 1000–1800 cm^{-1} region, the dark DRIFTS spectrum immediately before illumination ($t = 0$) were subtracted from the presented DRIFTS spectra. This removes the contribution from the water bending vibration at 1625–1630 cm^{-1}. In the 2500–4000 cm^{-1} region, the (smoothed) raw DRIFTS spectra from the catalyst were used. The background was collected in a 10-ml min^{-1} feed of 20% O_2 in N_2 (AGA research grade) on a (spectroscopically) clean TiO_2 sample unless stated otherwise.

2.4. MS

In the MS measurements, the QMS signal was calibrated by registering the $m/Z = 39$ signal for a known volume fraction of 500 ppm propane. From that level, the volume fraction of propane was decreased in 50-ppm steps. The drop in the QMS signal was recorded as a relative change, and a calibration curve was plotted with relative change in the $m/Z = 39$ signal as a function of the volume fraction drop of propane, thus giving a calibration curve valid throughout the concentration range used in the study. The $m/Z = 39$ signal was used instead of the main peak at $m/Z = 29$, because the latter was found to vary considerably depending on the reaction history of the MS chamber. In the same way, the $m/Z = 44$ signal was also measured and recorded as the relative change with the drop in the volume fraction of propane. The $m/Z = 44$ signal contains contributions from both propane and CO_2; however, by following the $m/Z = 39$ and 44 signals simultaneously, the contribution from propane in the $m/Z = 44$ signal was corrected, and the remaining part of the signal was used for monitoring CO_2. The rate of propane removal (CO_2 production) was calculated from the calibrated volume fraction C_x of propane (CO_2),

$$\frac{dn_x(t)}{dt} = \frac{PF}{RT}\left(C_{x,\mathrm{meas}}(t) - C_{x,\mathrm{feed}}\right)\ (\mathrm{mol\,s^{-1}}), \tag{1}$$

where $x = C_3H_8$ or CO_2, P denotes the total pressure (10^5 Pa), R is the molar gas constant, T is the gas temperature (293 K), and F is the gas flow rate (m^3/s). Average rates, $\overline{W}_x(N)$, for removal/production of species x ($x = C_3H_8$ or CO_2) were used to reduce the fluctuations in the data and to describe the rates not significantly affected by the rapid transients during the first minute in the PCO cycle (see Fig. 1). This facilitates the quantum yield to be determined in the region of saturation of the rate on reagent concentration, which also warrants the independence of quantum yield on photon flow [35]. $\overline{W}_x(N)$ is defined by the average momentary rates (Eq. (1)) during the last 2 min of the irradiation period N ($N = 1, 2, 3, 4$, and 5), according to

$$\overline{W}_x(N) = \overline{\frac{dn_x(t_N)}{dt}} \equiv \frac{1}{\Delta t}\int_{t_N}^{t_N+\Delta t} \frac{dn_x(t)}{dt}\,dt\ (\mathrm{mol\,s^{-1}}), \tag{2}$$

where $x = C_3H_8$ or CO_2, $t_N = 10N - \Delta t$ min (see Fig. 1), and $\Delta t = 120$ s. The carbon mass balance (CMB) was determined to elucidate and relate deviations in the total oxidation reaction ($C_3H_8 + 5O_2 \rightarrow 3CO_2 + 4H_2O$) to accumulation of surface species on the catalyst surface. The CMB is defined as

$$\mathrm{CMB}(t) \equiv \frac{1}{3}\frac{dn_{CO_2}(t)}{dn_{C_3H_8}} = -\frac{1}{3}\frac{dn_{CO_2}(t)}{dt}\bigg/\frac{dn_{C_3H_8}(t)}{dt}. \tag{3}$$

To remove fluctuations in the data, CMB(t) was calculated using a 10-point window average. The momentary CMB(t) and the average $\mathrm{CMB_{av}}$ obtained during the last 2 min of the irradiation interval N are distinguished to separate initial transients from long-term effects, where $\mathrm{CMB_{av}}$ is defined as

$$\mathrm{CMB_{av}}(N) \equiv \frac{1}{3}\frac{\overline{W}_{CO_2}(N)}{\overline{W}_{C_3H_8}(N)}. \tag{4}$$

2.5. UV light illumination

UV illumination was done using a 300-W Xe arc lamp source with a focusing lens assembly (Oriel). A 75-mm water filter was used to remove the infrared light and avoid

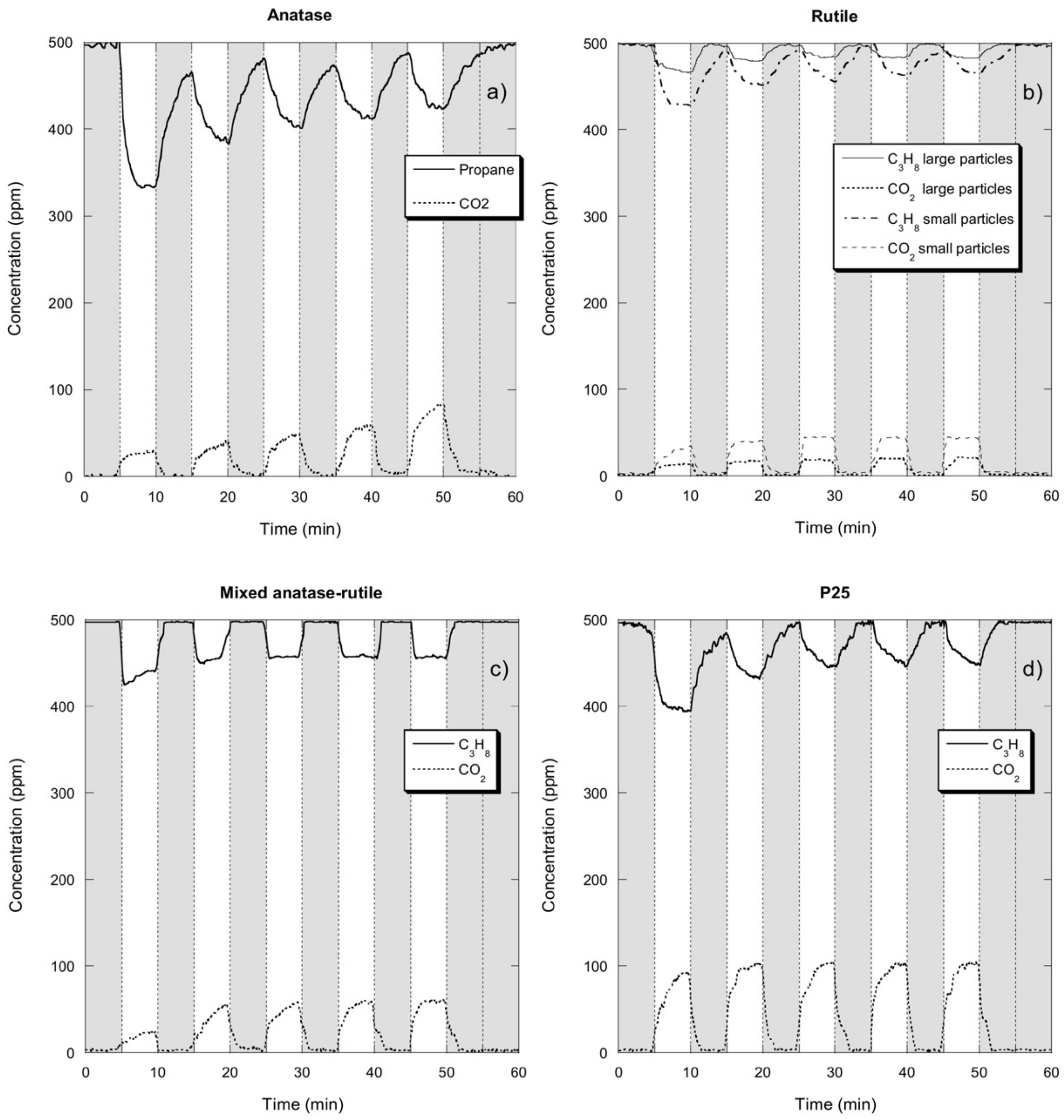

Fig. 1. Photocatalytic degradation of propane and evolution of carbon dioxide as a function of time on (a) anatase, (b) rutile (large and small particles [32]), (c) mixed anatase–rutile, and (d) P25. The measurements were made in flow mode (10 ml min^{-1}) with an initial propane concentration of 500 ppm in synthetic air, which was passed over the powder catalyst bed. The irradiation was made in cycles of 5 min (white area) followed by a 5 min dark period (grey area).

photon-induced heating of the sample. The UV light was guided through a fused silica fiberoptic bundle (Oriel) and directed into the reaction cell through a CaF_2 window. The total photon power at the sample was measured as 200 $\text{mW}\,\text{cm}^{-2}$ with a calibrated thermopile detector (Ophir). The incipient photon power above the band gap energy of TiO_2 was calculated from the total power and the spectral distribution of the radiance of the lamp source [17]. It was determined to be 16 mW/cm^2 (2.6×10^{16} $\text{photons}\,\text{cm}^{-2}\,\text{s}^{-1}$) for $\lambda < 386$ nm and 28 $\text{mW}\,\text{cm}^{-2}$ (4.8×10^{16} $\text{photons}\,\text{cm}^{-2}\,\text{s}^{-1}$) for $\lambda < 411$ nm, corresponding to the band gap energy of bulk anatase and rutile, respectively. Unless stated otherwise, the illumination was carried out stepwise, with 5 min of illumination followed by 5 min of darkness. A total of five illumination cycles were carried out.

3. Results

3.1. Online MS

Figs. 1a–1d show the measured QMS signal for the various TiO_2 samples used in the present study. The QMS signals in Fig. 1 were calibrated according to the procedure described in Section 2. The data in Fig. 1 demonstrate that all of the TiO_2 samples are able to convert propane to carbon dioxide under band gap illumination, in agreement with previous studies [4,14,15]. No other gas-phase products besides CO_2 and propane were detected, which in comparison with other studies, were notably small acetone has been observed [15], can be explained by the smaller propane concentration and the

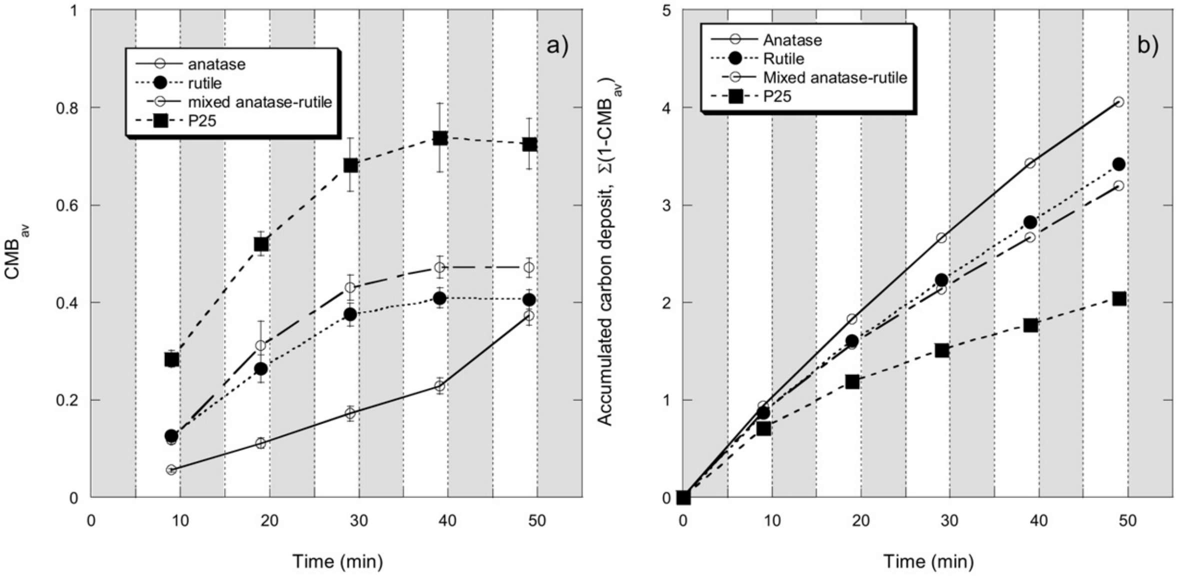

Fig. 2. (a) The average carbon mass balance $\mathrm{CMB}_{\mathrm{av}}$ as determined by Eq. (4) for anatase, rutile, mixed anatase–rutile, and P25. (b) The accumulated carbon deposit on the samples as defined by $\Sigma_N(1-\mathrm{CMB}_{\mathrm{av}})$. The white (grey) areas indicate the intermittent UV illuminated (dark) periods.

flow cell setup used here. The photoresponse varies between the different samples, and the turnover varies within and between illumination cycles for the same TiO_2 sample. All samples show a more pronounced dip in the volume fraction of propane during the first period of illumination. Anatase has an especially pronounced initial propane dip (Fig. 1a). The initial dips for the various TiO_2 samples do not correspond to an equally pronounced CO_2 production, demonstrating that surface-bound products are formed on TiO_2 in the course of the photoreaction. Finally, there is a systematic trend of increasingly more CO_2 evolution during the intermittent dark periods. This can be linked to a slow thermal reaction pathway, which scales with the amount of accumulated surface species and thus increases as a function of the illumination cycle (see below) [7]. In comparison with our previous study [7], are no initial dips in the C_3H_8 removal rate in the beginning of the first illumination cycle are apparent in Fig. 1. We ascribe this to the capillary colon used in the present study compared with the quartz capillary leak used in our previous study; in the colon, the dip is broadened and smeared out over time. Indeed, inspection of the first illumination period reveals a higher propane removal rate for each sample during the first minute of irradiation compared with subsequent illumination periods, in good agreement with an initially higher propane removal rate.

The accumulation of surface species is quantified in the CMB plot in Fig. 2, which explicitly shows that carbonaceous species accumulate on the surface during initial illumination periods. It is evident that surface species accumulate on all samples, but the mixed-phase anatase–rutile samples (P25 and own mix of anatase–rutile) have the highest conversion of propane to CO_2. Interestingly, the anatase sample exhibits the poorest initial total oxidation. Even after 25 min of illumination, the anatase is inferior to rutile, even though it steadily approaches that of rutile and surpasses rutile after >30 min of illumination (not shown). This is interesting, because anatase is commonly accepted as the more photoactive of the two polymorphs. The high initial photocatalytic degradation rate of anatase apparent in Fig. 1 is due instead to photo-oxidation of propane to stable surface intermediates in combination with the high surface area of anatase; it is generally easier to prepare high-surface area anatase than rutile (see Table 1).

Taking the surface area into account, it is clear that the amount of CO_2 produced is lowest on anatase and is highest by far on P25. Fig. 3 shows the reaction rate determined from Eq. (1) normalized to the total illuminated catalyst surface area. The illuminated surface area is estimated from the specific surface area, S_{BET}, in Table 1 and the UV light penetration in the porous TiO_2 powder bed, which is set at 1 μm [36]. It is evident that even in absolute numbers, the amount of CO_2 produced over anatase per unit area of illuminated catalyst is comparable to that over rutile. Thus, a high-surface area rutile sample is predicted to have an absolute CO_2 turnover exceeding that of anatase. We have experimentally verified this. Fig. 1b also shows the QMS response for a rutile sample with a BET specific area of 195 m^2/g. Even if the turnover does not scale proportional to the specific area, the turnover is clearly improved compared with that of the rutile sample with lower surface area. Finally, we estimate a lower limit of the turnover number (TON), defined as the ratio of the number of propane molecules that are photoconverted to CO_2 over the illuminated powder bed during 25 min of illumination to the number of photocatalytic sites. As an upper limit, we take the number of photocatalytic centers to be the same as the TiO_2 cation density, $N = 5 \times 10^{14}\ \mathrm{cm}^{-2}$ [23], and calculate the total number of photocatalytic centers as $N_{\mathrm{T}} = N \times S_{\mathrm{BET}}$. However, it is likely that the true number of photocatalytic active sites is orders of magnitude lower [35], which means that the foregoing estimate is a gross underestimation of TON. Integrating the data in Fig. 3 gives TON = 9, 15, 8, and 112 for anatase, rutile, mixed anatase–rutile, and P25, re-

Table 1
Physical properties of the TiO_2 samples prepared by hydrothermal treatment of microemulsions [31–33]

TiO_2 polymorph	BET area (m^2/g)	Particle size from TEM (nm)[a]	Particle size from XRD (nm)[b]	Pore size maximum (Å)[c]	Optical absorption edge (nm)[g]
Anatase	260	15	14	35	375
Rutile[d]	40	6×80	8	50	400
Rutile[d]	195	3 × 5	5	50	388
Anatase–rutile mix[e]	260	15	14	35	375
P25[f]	40 (50)	–	30 (21)	20 (narrow)/200 (broad)	380

[a] After 3 photooxidation cycles, each 20 min long.

[b] Obtained from the Scherrer equation.

[c] Obtained from BJH analysis of the isotherm (desorption).

[d] The primary "rodlike" rutile particles are elongated with varying lengths and width, which aggregates into 200–1000 nm sized bundles [27,29]. The (110) facet is the mostly exposed crystal facets on the larger rutile particles. The smaller particles expose a significant fraction of (101) facets. The absorption edge shifts down with decreasing particle size [32].

[e] Mixture of anatase (80 at%) and rutile particles (20 at%) was prepared analogous to pure anatase but with slightly different hydrothermal treatment conditions. The reported dimensions represent the anatase particles.

[f] Specific area and primary particle size, respectively, as specified by the supplier (Degussa) in paranthesis.

[g] Optical abortion edge as determined from a plot of $(Ah\nu)^{1/2}$ vs $h\nu$.

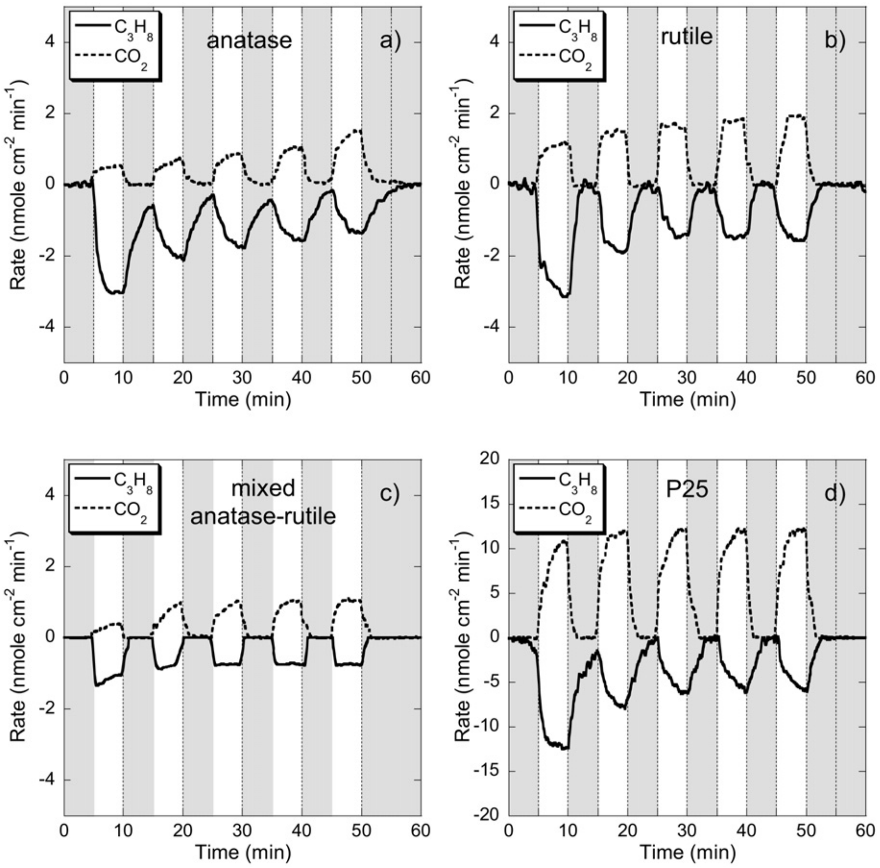

Fig. 3. The surface area normalized reaction rate determined from Eq. (1) for (a) anatase, (b) rutile, (c) mixed anatase–rutile, and (d) P25. A positive (negative) value indicates formation (removal) of the species.

spectively. This conservative estimate of TON confirms that the photo-induced reactions on the TiO_2 samples are catalytic reactions [35]. The relative TONs for the different TiO_2 samples are in good agreement with the trend obtained from the CMB data (Fig. 2) and show that the TON is lowest for anatase and highest for P25. We attribute the reversed order in the trend of TON compared with CMB for rutile and mixed anatase–rutile due to uncertainty of estimating N_T. For comparisons, the corresponding photonic efficiencies [35] were calculated to be 0.015, 0.005, 0.011, and 0.048 molecules photons^{-1} for anatase, rutile, mixed anatase–rutile and P25, respectively, during the last 2 min of the first illumination period. Comparing the TON with the photonic efficiency clearly shows that the major trend difference is (as expected) due to surface area normalization, which enhances the TON for rutile compared with that for anatase.

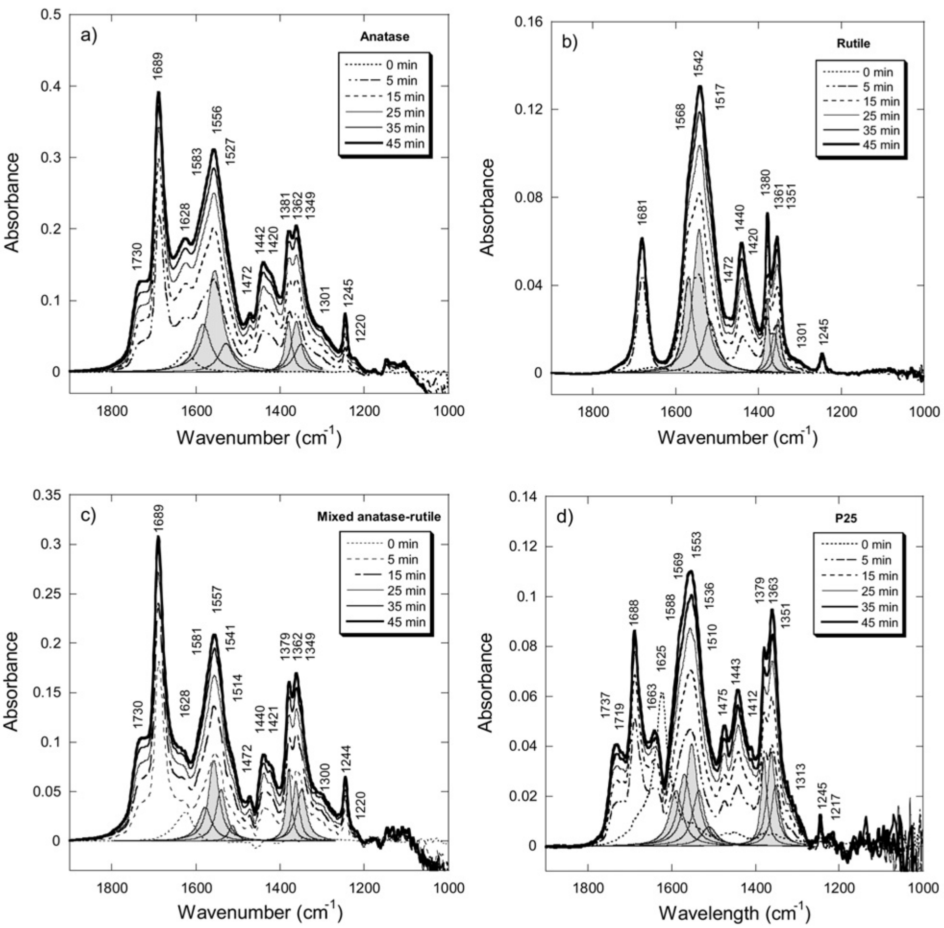

Fig. 4. Diffuse reflectance infrared spectra in the 1000–1900 cm^{-1} region obtained at different times (0–45 min) during photooxidation of propane on (a) anatase, (b) rutile, (c) mixed anatase–rutile, and (d) P25, respectively. The grey areas show the deconvoluted Lorentzian peaks in the ν_a(OCO) and ν_s(OCO) regions due to μ-formate, μ-acetate, and aqueous formate. The peak fitting was done with a minimum number of peaks associate with clearly resolvable peaks (fixed $\pm 5\ \text{cm}^{-1}$) in the spectra only and was minimized over the full time-domain (0–45 min) using spectra acquired every 5 min. Spectra of TiO_2 samples in synthetic air prior to illumination were used as background in each measurement.

3.2. DRIFTS

DRIFTS was used to gain insight into the nature of the surface species formed in the course of the photoreactions in situ. Figs. 4 and 5 show a few selected DRIFTS spectra acquired at the end of each illumination cycle. The spectra were acquired simultaneously with the QMS spectra shown in Figs. 1a–1d. The DRIFTS spectra were recorded every 30–50 s in the course of the reaction. The spectra recorded at $t = 0$ min were recorded in dark with gas-phase propane in equilibrium with the surface. In Fig. 4, each spectrum recorded at $t > 0$ is subtracted from the corresponding spectrum recorded at $t = 0$ min to show only the surface species formed due to photon irradiation. Fig. 5 shows the (smoothed) raw DRIFTS spectra in the 2500–4000 cm^{-1} region. The main peak visible in the dark in the 1800–1000 cm^{-1} region before illumination occurs at around 1625 cm^{-1} due to the δ(HOH) vibrational mode in small amounts of adsorbed water. This was independently confirmed by leaking controlled amount of water vapor onto dry TiO_2 powder.

In the dark, propane binds only weakly to TiO_2. The DRIFTS spectra show that most of the propane desorbs from the TiO_2 surfaces at 293 K when the sample is evacuated or flushed in synthetic gas. Propane does not dissociate on anatase at 293 K. At $T > 360$ K, absorption bands due mainly to acetone appear in the DRIFTS spectra after 30 min of propane exposure (not shown), in agreement with our previous findings [7]. In contrast, on rutile, small amounts of acetone appear already at 293 K. In fact, all samples containing rutile, even the mixed samples, exhibit peaks associated with acetone after the initial dark stabilization period in propane. This is evident in the nonsubtracted spectra shown in Fig. 5 (2984 cm^{-1} peak). This finding indicates that the reactivity of the propane/TiO_2 adsorption system is structure-sensitive and is related to the TiO_2 crystal modification. At present, we cannot assign this to either the presence of a particular crystal face or to special defect sites (e.g., O adatoms, O vacancies, Ti^{3+} sites) present on rutile, or to combinations of the two. It should be noted, however, that the number of defects or low-coordinated Ti sites are expected to be higher on the anatase particles due to their smaller size (Table 1).

The spectra obtained during UV illumination of the different materials have several peaks in common, but there also are some specific differences between the different polymorphs of TiO_2. The peaks that they have in common (even if they

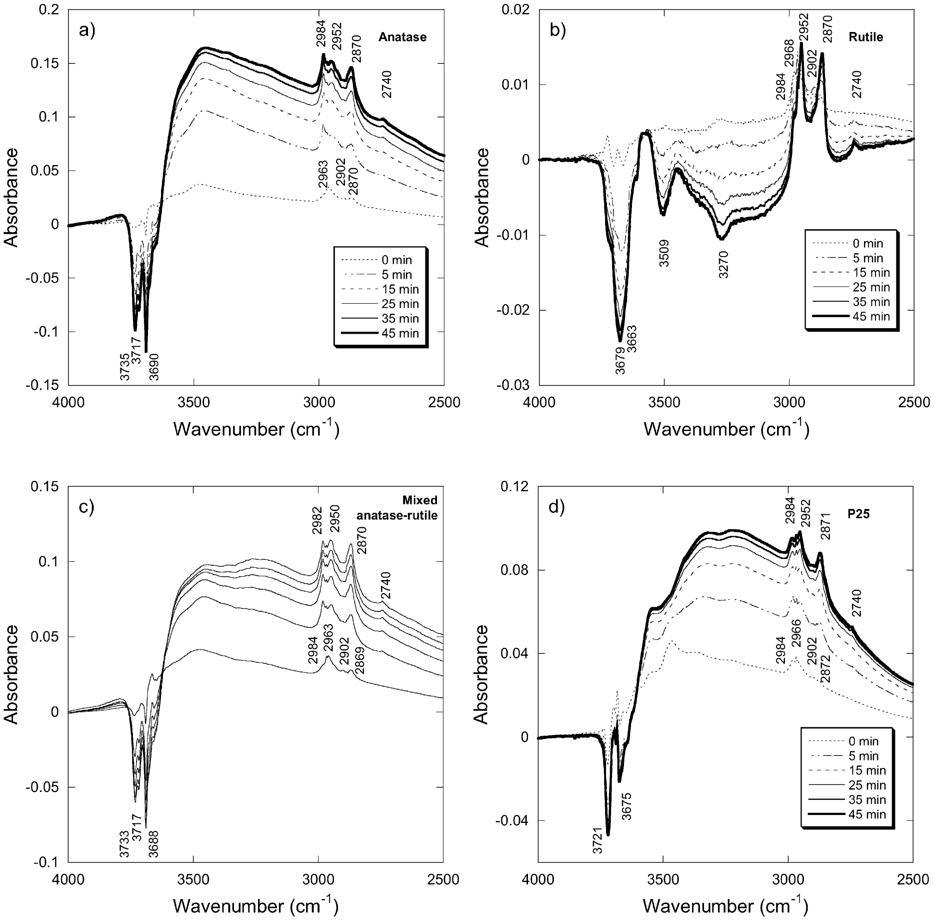

Fig. 5. Diffuse reflectance infrared spectra in the 2500–4000 cm^{-1} region obtained at different times (0–45 min) during photooxidation of propane on (a) anatase, (b) rutile, (c) mixed anatase–rutile, and (d) P25, respectively. The negative ν(OH) bands are associated with Ti–OH groups that are present on the initially prepared TiO_2 samples and indicate that these species are depleted during the experiments. Spectra of TiO_2 samples in synthetic air prior to illumination were used as background in each measurement.

are shifted slightly with respect to one another) are located at around 1689, 1555, 1440, 1380, 1360, and 1245 cm^{-1}. Similarly, pronounced peaks occur at ca. 2983 cm^{-1} (strong on the anatase sample), 2952 cm^{-1} (strong on all samples), 2870 cm^{-1} (strong), and 2744 cm^{-1} (medium). Peaks that exist mainly on anatase occur at ca. 1735, 1472, 1420, 1150, and 1106 cm^{-1}, whereas the peak at 1568 cm^{-1} can be seen (as a shoulder to the 1541 cm^{-1} peak) mainly on the sample with pure rutile crystal structure. In addition, the P25 sample exhibits clearly distinguishable peaks at ca. 1719 and 1663 cm^{-1}. Fig. 5 shows negative ν(OH) vibrational bands in the 3600–3700 cm^{-1} region, indicating that Ti–OH species are depleted during illumination. These bands are similar to those observed elsewhere [7,37,38] and are attributed to Ti–OH species in different chemical environments. In analogy with previous studies, the loss of the ν(OH) vibrational modes suggest that these groups either are consumed during the photoreaction or bond to dissociation fragments (such as methyl groups [39]).

Most of the vibrational absorption bands apparent in Fig. 4 can be readily identified with the acetone (2984, 1680–1690, and 1245 cm^{-1}), R–COO^- species, and formate species in particular (∼1500–1600 and ∼1350–1380 cm^{-1}) [8,9,11,17,24,29,40–45]. In what follows, we scrutinize the spectral information in detail and identify key surface intermediates on each sample. To facilitate the peak assignments in Fig. 4, we make comparisons with measurements on several candidate adsorption systems representing likely surface intermediates on the same set of samples. We have reported results for acetone adsorption on TiO_2 elsewhere [11,17].

Fig. 6 shows DRIFTS spectra obtained after HCOOH gas-phase adsorption (solid lines) on anatase, rutile, and P25. Formic acid adsorption has been studied in detail on rutile [23–26,29,32]. It has been shown that on the rutile (110) surface, the carboxylic proton is dissociated and binds to bridging O atoms, whereas formate (HCOO) binds to Ti sites (with μ-coordination) [24,26]. The spectra shown in Fig. 6 agree well with these previous studies, and the peaks at ca 1536 and 1362 cm^{-1} can be assigned to the ν_{as}(OCO) and ν_s(OCO) modes of μ-formate, respectively, whereas the peak at 1377 cm^{-1} can be assigned to the corresponding δ(C–H) mode. But inspecting the spectra more closely reveals that the shoulder on the 1536 cm^{-1} peak apparent at 1563 cm^{-1} contains a contribution from another type of μ-formate species [32]. It can be assigned to the ν_{as}(OCO) mode of formate bonded with one O atom in an O vacancy site in the rutile structure [24]. The corresponding symmetric mode has been reported to occur at

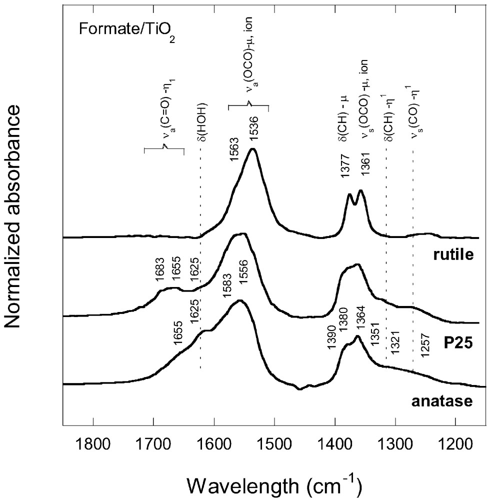

Fig. 6. DRIFT spectra obtained after formic acid adsorption (7900 ppm in 100 ml min^{-1} synthetic air) on rutile, P25 and anatase at 293 K. The spectra were acquired after 25 min dosing and subsequent 10 min in a flow of synthetic air.

~1390 cm^{-1} [24] but is too weak to be unambiguously resolved in our spectra. We note, however, that unambiguous mode assignment is intrinsically more difficult in the 1350–1390 cm^{-1} region than in the ν_{as}(OCO) region (1500–1600 cm^{-1}) due to the intense contribution from the δ(C–H) vibrational modes in various formate and bicarbonate species (see below). Moreover, contributions from formate species bonded in different geometries may occur; for example, the ν_s(OCO) mode in μ-formate bonded to (101) rutile facets occurs at 1387 cm^{-1} [32]. The DRIFTS spectra obtained after formic acid adsorption on anatase reveal, in addition to μ-formate (peaks at 1550, 1380, and 1364 cm^{-1}), monodentate formate (η^1-coordination) with absorption bands at around 1683, 1655, 1320, 1300 and 1260 cm^{-1}, demonstrating that that at least two major types of η^1-coordination exist in different adsorption environments [21] (probably to defect sites, edges, etc., because the concentration of η^1-fromate scales with particle size [32]). Aqueous-phase formate ions are clearly distinguishable on anatase at high coverage with major peaks at 1582, 1391, and 1351 cm^{-1}, in good agreement with previous studies [29], and scales with the water coverage. The contribution of aqueous formate is much weaker on rutile and can be explained by the lower water coverage observed on the rutile samples (see Fig. 4).

Fig. 7 shows DRIFTS spectra acquired after CO_2 reactive adsorption on rutile in the dark as a function of catalyst temperature up to 443 K. To promote carbonate formation, the experiments were carried out with an addition of water vapor in a feed of 1% CO_2 in synthetic air. Apart from variations in the reflectivity between samples and different temperatures (with sharp emission bands at ~1550 and ~1330 cm^{-1} at elevated temperatures, which interfere with the ν(OCO) absorption bands), absorption bands are seen in the 1550–1570, 1440–1444, 1425–1430, and 1375–1385 cm^{-1} regions, which we assign to bicarbonate complexes in a mixed water (deuterium) layer. The absorption band at ~1440 cm^{-1} is present in both cases and appears only after water (deuterium) is desorbed from the surface at elevated temperatures (dip at ~1630 cm^{-1}). We tentatively attribute this peak to a ν(CO) mode in a surface-coordinated bicarbonate species (rather than carbonate), because it correlates with the 1369 cm^{-1} peak present in H_2O only, suggesting that it is related to a isotope shift (tentatively the δ(CH) mode in bidentate bicarbonate).

It is clear from the analysis of the simpler adsorption systems that the main absorption bands visible in the DRIFTS spectra in Fig. 4 can be explained by photon-induced acetone and formate formation on both anatase and rutile. Subsequent reactions with H_2O lead to (bi)carbonate formation. In addition, a weak absorption band appears in the 1515–1530 cm^{-1} region depending on the TiO_2 phase, which is attributed to the ν_a(OCO) mode in acetate ions [18,29]. The absorption band at ~1730 cm^{-1} in Fig. 4 is seen only on anatase particles and correlates with corresponding peaks at ~3180 and ~1220 cm^{-1}, and can (in analogy with previous studies) be tentatively attributed to formic acid molecules weakly adsorbed through hydrogen bonding [ν(C=O), ν(OH), and ν(CO)] [10]. The appearance of vibrational bands associated with aqueous $HCOO^-$ and CH_3COO^- ions is qualitatively consistent with the higher concentration of molecular water detected on anatase with its

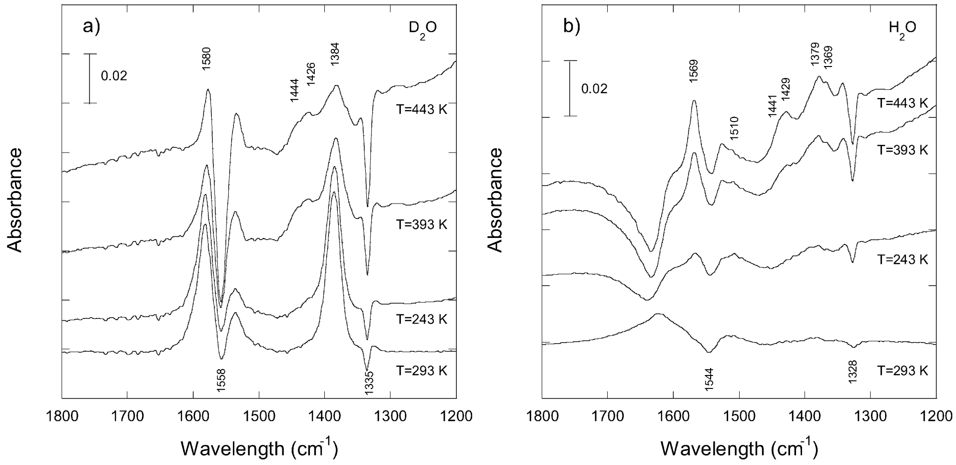

Fig. 7. DRIFT spectra recorded at the indicated sample temperatures after reactive CO_2 adsorption on rutile in humidified reaction gas using (a) D_2O and (b) H_2O mixed in synthetic air.

Table 2
Compilation of infrared absorption bands and vibrational mode assignment of the major adsorbed species on TiO$_2$ formed during photocatalytic degradation of propane. Assignments are based on the reported DRIFT data in the present study and the following references: [8–10,18,19,21,24,29,40–42,45,47]

TiO$_2$ polymorph	Surface specie	Mode description	Frequency (cm^{-1})
Anatase	Acetone	ν(C=O)	1689, 1650 (defects)
		ν(C–C)	1245
		δ_a(CH$_3$)	1421
		ρ(CH$_3$)	1136
	Formate (μ-coordinated)	ν_a(OCO)	1556
		ν_s(OCO)	∼1364
		δ(CH)	1380
	Formate ions (aqueous)	ν_a(OCO)	1583
		ν_s(OCO)	∼1351
		δ(CH)	∼1390
	Formate (η^1-coordinated)	ν_a(OCO)	1655–1683
		ν_s(OCO)	∼1260
		δ(CH)	∼1320
	Formic acid (H-bonded)	ν(CH)	2744
		ν(OH)	∼3180
		ν(C=O)	1735
		ν(CO)	∼1220
	Carbonate (μ-coordinated)	ν(C=O)	1663
		ν_a(OCO)	1212
	Bicarbonate	ν_s(OCO)	1435
Rutile	Acetone	ν(C=O)	1681, 1669 (defects)
		ν(C–C)	1245
	Formate (μ-coordinated A/B)	ν_a(OCO)	1536/1563
		ν_s(OCO)	1361/not resolved
		δ(CH)	1377
	Acetate	ν_a(OCO)	1518
		ν_s(OCO)	1425
	Bicarbonate (ion)	ν_{as}(OCO)	1550–1570
		ν_s(OCO)	1435–1442
		δ(OH···H)	1367

smaller pore size distribution. Table 2 compiles the observed vibrational frequencies and mode assignments deduced from the acetone, formic acid, and reactive CO$_2$ adsorption experiments.

To compare the relative abundance of the main surface intermediate and relate the DRIFTS data to the QMS results given in Section 3.1, the absorbances due to acetone (1681–1689 and 1245 cm^{-1}), μ-formate (1536 and 1557 cm^{-1} for rutile and anatase, respectively), aqueous formate (1583 cm^{-1} on anatase only), acetate (1515–1530 cm^{-1}), and the sum of the acetone, total formate, and acetate concentration were extracted. (The smaller η^1-formate contribution on the anatase-containing samples was neglected due to the interfering water and carbonate peaks occurring in the same region.) The comparison was done by applying a consistent peak deconvolution procedure for each set of absorbance curves on each sample. Thus, a series of absorbance curves obtained as a function of illumination time (of which those presented in Fig. 4 are examples) were fitted with a common set of Lorentzian curves in the 1400–1800 and 1245 cm^{-1} regions—one set for anatase with fixed (±5 cm^{-1}) peak positions representing μ- and aqueous formate, acetone, acetate, and water; one set for rutile with fixed peak positions representing μ-formate, acetone, acetate, and water; and one set for the mixed-phase samples containing both fixed anatase and rutile peaks. As an example, the resulting curve fits obtained after 15 min of illumination are designated by gray areas in Fig. 4.

Because the surface area and reflectivity vary among the materials, there is a need to normalize the spectra consistently to be able to cross-compare the relative surface concentrations on each sample. This is normally done by ratioing a changing reaction-dependent absorption band against a constant band [46]. Here we normalized against the integrated absorbance in the 3015–2750 cm^{-1} ν(CH) stretching region at $t = 0$ (before illumination) on each sample. As discussed above, this band is due to propane for anatase and to propane with small amounts of acetone for rutile. We assume that variation in the hydrocarbon coverage, θ_{CH}, at $t = 0$ is not too large on the different TiO$_2$ samples, so that we can use θ_{CH}, ($t = 0$) as a common fixed reference point. The integrated value obtained in this manner, I_{CH}, is proportional to the number of adsorbed hydrocarbon molecules, N_{CH}, where $N_{CH} \propto A_{CH}\theta_{CH}$ and $A_{CH} = A_{CH}(d_{CH})$ is the total surface area of the analyzed sample within a penetration depth, $d_{CH} = d_{CH}(\bar{\nu})$, of the powder bed at wavenumber $\bar{\nu}$, and θ_{CH} is the number of absorbers per unit area. As usual, we use the ratio of the absorption coefficient (k) and scattering coefficient (s), k/s, to describe the diffuse reflectance properties of TiO$_2$, which may be different for the different TiO$_2$ samples. The quantity k/s is in a first approximation proportional to the measured absorbance for TiO$_2$. Thus we write an expression that approximates the measured (absolute) absorbance in terms of number of hydrocarbon molecules (as measured by the absorption at 3015–2750 cm^{-1}) and specific TiO$_2$ sample,

$$I_{CH} \propto a' N_{CH} = a' A_{CH}\theta_{CH}, \tag{5}$$

where $a' = k'/s'$. Note that I_{CH} is an indirect measure of the surface area. Normalizing the contribution, $I(x)$, of species x at wave number $\bar{\nu}$ (obtained through Lorentzian curve fitting) to the total hydrocarbon ν(C–H) absorbance I_{CH} at $t = 0$ gives

$$I_{norm}(x) = I(x)/I_{CH} = a'' A_x \theta \big/ \big(a' A_{CH}\theta_{CH}\big) = aA\theta(x)/\theta_{CH}, \tag{6}$$

where $a = a''/a'$ and $A = A_x/A_{CH}$. Now with this "intraparticle" normalization, aA can, to a good approximation, be assumed to be the same for all samples, because the infrared signal of each chemical species is affected in the same way by diffuse scattering on each TiO$_2$ sample irrespective of the size or structure-dependent properties in the reflectance signal. Note, however, that the above analysis yields only the calibrated trends, not absolute values of adsorbate coverages. Independent measurements are needed for this purpose. The relative coverage, $R_i(x(t))$, of species x at time t for sample i can be obtained by comparing the ratio of $I_{norm}(x)$ to a common reference, because the factor sA cancels out in Eq. (6). In what follows, we use the P25 sample at $t = 25$ min illumination as a reference. Thus, by definition,

$$R_{P25}\big(x(t = 25\text{ min})\big) = I^{P25}_{norm}\big(x(t = 25\text{ min})\big) \big/ I_{REF} \equiv 1. \tag{7}$$

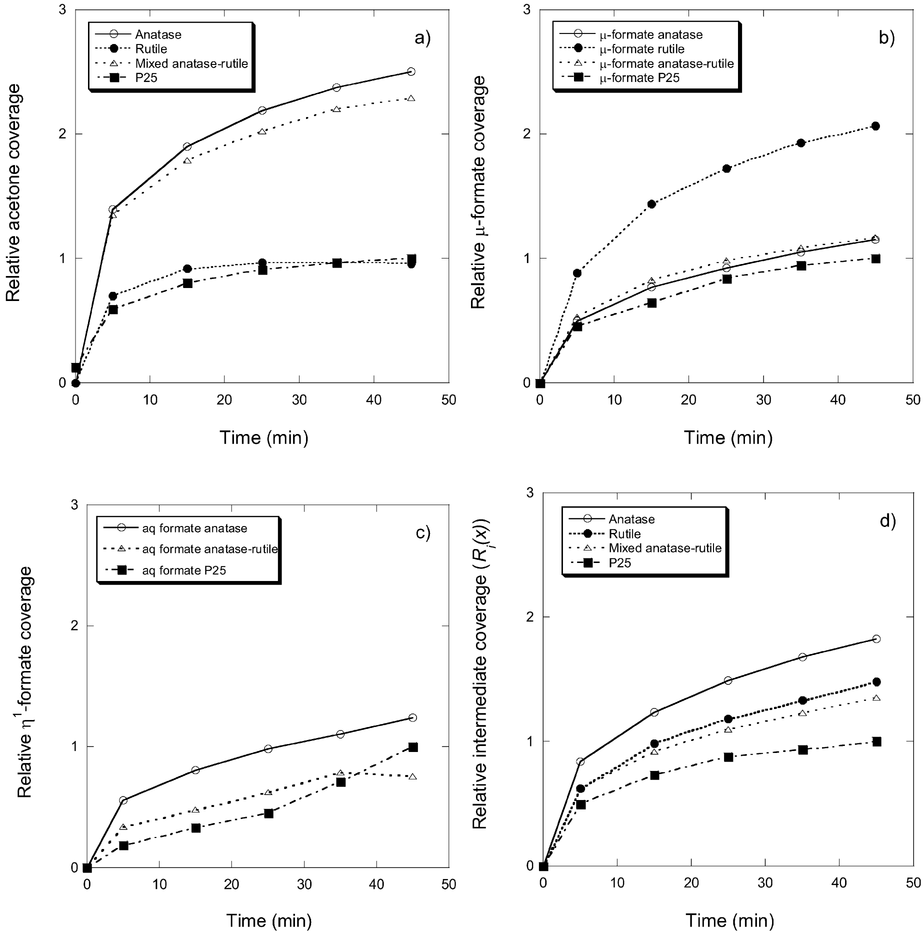

Fig. 8. The relative coverage ($R_i(x(t))$) of the main intermediates as a function of illumination time deduced from the DRIFT experiments using Eq. (7): (a) η^1-acetone, (b) μ-formate, (c) aqueous formate, and (d) sum of acetone and formate.

Fig. 8 shows the relative coverage of the main intermediates according to Eq. (7), omitting η^1-formate for the reasons discussed above. From Fig. 8, it can be seen that the acetone coverage is about 2–3 times higher on anatase and mixed anatase–rutile than on rutile and P25 at all times during illumination. Conversely, the μ-formate coverage is 2–3 higher on rutile than on all other samples, whereas aqueous formate is absent on rutile. This suggests that the rate-determining step is the photocatalytic oxidation of acetone on anatase and of formate on rutile.

From the foregoing analysis, we conclude that the coverage of surface intermediate is largely given by the sum of the acetone and formate coverage, as plotted in Fig. 8d (neglecting the smaller contributions from acetate and η^1-formate). It is seen that during the initial 25-min illumination period, the concentration of surface intermediates is lowest on P25 and increases in the order P25 < mixed anatase–rutile < rutile < anatase. This is in perfect agreement with the results from the carbon mass balance analysis shown in Fig. 2b. This assertion is quantified in Fig. 8, which plots the concentration of accumulated surfaces species deduced from the QMS (Fig. 2b) versus the surface intermediates obtained in the DRIFTS measurements (Fig. 8d). The slightly larger than unity slope in Fig. 9 can be readily explained by the exclusion of some minor surface species not included in the DRIFTS analysis shown in Fig. 8d. Note also that the linearity in Fig. 9 provides further support for our peak calibration procedure.

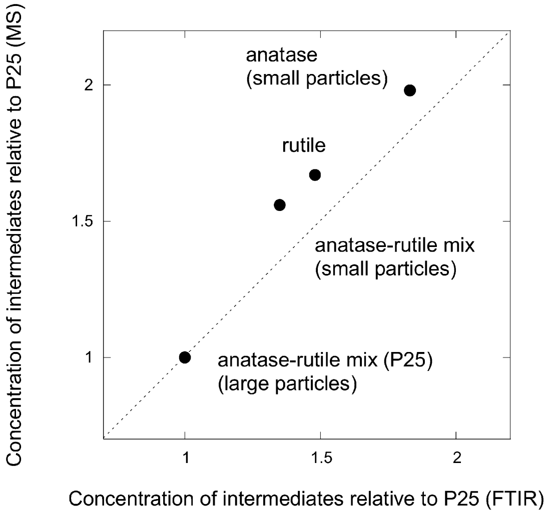

Fig. 9. Accumulated carbon concentration of surface intermediates as obtained from mass spectrometry using the relation $\Sigma(1 - \mathrm{CMB}_{\mathrm{av}})$ versus accumulated concentration of main surface intermediates obtained from the calibrated FTIR data. In each case the data has been normalized to the P25 data.

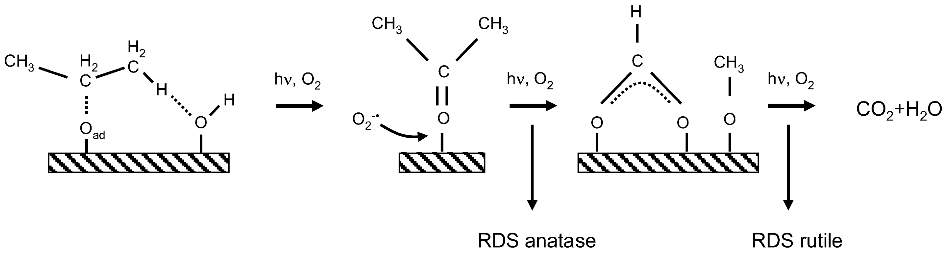

Fig. 10. Schematic drawing of the proposed propane photooxidation mechanism deduced from the FTIR data, which explicitly shows the different rate determining steps (RDS) observed on anatase and rutile TiO_2, respectively.

4. Discussion

The qualitative results in the previous section of the photo-oxidation of propane over TiO_2 are in perfect agreement with the previous studies referred to in Section 1 and can be readily explained by the main trends for the photo-oxidation of alkanes on TiO_2 discussed elsewhere [4,7,11,13,14]. However, the comparative approach between anatase and rutile used here facilitates a more comprehensive molecular understanding than what has been available previously. In particular, the measured gas-phase product distribution can be understood and correlated with surface intermediates, which are both identified and quantified. The significance of our results is summarized in Fig. 9, which connects the measured gas-phase oxidation rate to (identified) surface species. The proportionality between the two data sets shown in Fig. 9 not only proves that the oxidation of intermediate surface species (not propane) is rate-determining for all samples, but also identifies the rate-determining step and the surface species involved (Fig. 10). This suggests that the difference between the different nanoparticle systems is not due primarily to different interfacial charge transfer properties, as is commonly discussed in the literature [5]. Thus, the accumulation of surface species is directly related to the propane → CO_2 conversion rate and increases in the order anatase $<$ rutile $<$ mixed-phase anatase $<$ P25 over the first 5×5 min illumination periods and can be correlated with the slowest reaction step in each case. The same trend—that rutile has higher TON than anatase and that P25 is the most efficient photocatalyst—also can be deduced from the estimated TON. We note that TONs correspond to the DRIFTS data better than do the photonic efficiency data, because the latter neglects the different surface areas of the catalysts. A detailed spectroscopic analysis of the surface intermediates reveals that the photo-oxidation of propane on TiO_2 is structure-sensitive. Our data provide clear evidence that bridging bidentate species (primarily μ-formate) are the key surface species that accumulate on rutile after extended illumination, and that the oxidation of these species is the rate-determining surface reaction step for the total oxidation of propane. In the case of anatase, it is the photo-oxidation of acetone that is slow and is responsible for the initial high concentration of intermediates and the small CMB (Fig. 2). On anatase, formate (η^1- and μ-coordinated) eventually forms after oxidation of acetone. Formic acid dissociates directly on the (110) planes [23,24] and explains the finding that μ-formate is detected almost exclusively in FTIR, because rutile exposes large “single-crystal”-like (110) facets [29,32]. This argument is supported by our recent findings that rutile particles of much smaller size than what is normally available do indeed give rise to significant amounts of η^1-formate on formic acid adsorption [32]. Fig. 10 summarizes the spectroscopic findings.

It is intriguing that our anatase sample containing small (14 nm) particles has an inferior catalytic activity (TON) compared with rutile, because anatase is commonly considered the more active photocatalyst of the two polymorphs. Even though the propane removal rates and CO_2 production rates are similar, the CMB is better for rutile over the first 5 illumination cycles (Fig. 2). This correlates with the greater accumulation of intermediates on anatase, particularly acetone (Figs. 8 and 9). The results from the mixed anatase–rutile sample (containing $>80\%$ anatase) show that the presence of both anatase and rutile enhances the CMB more than what would be expected from extrapolating the sum from the contributions from anatase and rutile, respectively. Again, our DRIFTS data demonstrate that this can be traced to the lower rate of intermediate deposits on the surface. Because the physical properties of the anatase and mixed anatase–rutile samples are similar (with the same synthesis method and same anatase particle size), we can conclude that there is a synergetic action between the anatase and rutile particles, where, for example, surface diffusion between rutile and anatase is important and the beneficial effects of acetone dissociation are effective for rutile. The smaller these rutile particles are, the better this effect, because then formation of strong μ-coordinated formate is avoided in favor of η^1-coordinated formate [32]. We propose that a similar synergetic action is also present on P25, which contains a similar small fraction of rutile particles.

Furthermore, the same qualitative trends in the intermediate concentration distribution are found on the anatase and mixed anatase–rutile samples. In particular, there is a correlation between the high concentrations of acetone on these samples. It is tempting to correlate the high acetone concentration to energetically favorable adsorption sites due their small particle size (e.g., lattice defects), because the corresponding acetone concentration is lower on both the (low-surface area) rutile and P25 samples, in which the particle sizes are significantly larger. Thus, one might speculate that acetone adsorbs in particularly stable η^1-coordinated acetone species bonded to defect sites on the anatase samples. We cannot find spectroscopic support for this explanation, however. It is known that the $\nu(C{=}O)$ frequency is sensitive to the local bonding [17,47], but Fig. 4 shows that the $\nu(C{=}O)$ vibrational mode in P25 occurs at the same frequency as on the anatase and mixed anatase–rutile samples. In contrast, the higher reactivity of the rutile sample toward acetone correlates with a stronger coupling of the carbonyl to the Ti(5) surface atom [a downshift of ν(C=O) of 8 cm^{-1} compared with anatase]. Other factors may also contribute to the different acetone reactivity on the anatase and rutile particles, however. A higher thermal reactivity toward 2-propanol for the rutile (001) surface compared with the (110) surface has been attributed to the closer proximity of bridging O atoms on the (001) surface [48]. In either case, our results point to the beneficial effect of large anatase particles in the photo-oxidation of propane, and aliphatic compounds in general, in which ketones are common oxidation products. These results suggest that the large particle size of the anatase in P25 compared with our mixed anatase–rutile sample is another reason why P25 is a better photo-oxidation catalyst than the smaller 14-nm anatase particles.

5. Conclusion

The photocatalytic oxidation of propane over anatase and rutile nanoparticles was studied by simultaneous in situ DRIFTS and QMS. The conversion of propane leads to accumulation of surface intermediates on the TiO_2 surface. The oxidation of these intermediates is rate-determining for the full propane oxidation and is directly correlated with the TON. The accumulated carbon concentration determined from the gas-phase carbon mass balance is proportional to the concentration of intermediate surface species measured independently and simultaneously with FTIR. Carbon mass balance and TON increase in the order small anatase < large rutile < small rutile < mixed anatase–rutile < P25, where the difference between the mixed anatase–rutile and the P25 samples is mainly the larger anatase particle size in P25. The intermediate surface species are identified by a detailed comparison with spectra measured on candidate adsorption systems. Propane oxidation is structure-sensitive and gives rise to different limiting intermediates on anatase and rutile. Propane is converted to acetone on both surfaces. On anatase, acetone oxidation is slow and is gradually converted to formate. In contrast, on rutile, acetone readily oxidizes to formate. On both surfaces, primarily μ-coordinated formate forms as acetone oxidizes. The concentration of monodentate species increases with decreasing particle size, notably η^1-formate on anatase. The reactivity of the mixed-phase anatase–rutile TiO_2 is greater than what would be expected from the individual particles and suggests a synergetic action between anatase and rutile particles.

Acknowledgments

The work was funded through the Swedish Ministry of Defence (project 430-A4515). The authors thank M. Andersson and A.E.C. Palmqvist for sample preparation.

References

[1] A. Fujishima, K. Hashimoto, T. Watanabe, TiO_2 Photocatalysis—Fundamentals and Applications, BKC, Tokyo, 1999.
[2] A.L. Linsebigler, G. Lu, J.T. Yates Jr., Chem. Rev. 95 (1995) 735.
[3] A. Mills, S. Le Hunte, J. Photochem. Photobiol. A 108 (1997) 1.
[4] J. Peral, X. Domenech, D.F. Ollis, J. Chem. Technol. Biotechnol. 70 (1997) 117.
[5] O. Carp, C.L. Huisman, A. Reller, Prog. Solid State Chem. 32 (2004) 33.
[6] M.L. Sauer, D.F. Ollis, J. Catal. 163 (1996) 215.
[7] C. Hägglund, B. Kasemo, L. Österlund, J. Phys. Chem. B 109 (2005) 10886.
[8] A.A. Davydov, Infrared Spectroscopy of Adsorbed Species on the Surface of Transition Metal Oxides, Wiley, New York, 1990.
[9] G. Busca, Catal. Today 27 (1996) 457.
[10] A.A. Davydov, Molecular Spectroscopy of Oxide Catalyst Surfaces, Wiley, Chichester, 2003.
[11] L. Österlund, A. Mattsson, in: L. Vayssieres (Ed.), Solar Hydrogen and Nanotechnology, vol. 6340, SPIE, 2006, p. 1.
[12] M. Formenti, F. Juillet, P. Meriaudeau, S.J. Teichner, Chem. Technol. 1 (1971) 680.
[13] N. Djeghri, M. Formenti, F. Juillet, S.J. Teichner, Faraday Discuss. Chem. Soc. 58 (1974) 185.
[14] S.J. Teichner, M. Formenti, in: M. Schiavello (Ed.), Photoelectrochemistry, Photocatalysis, and Photoreactors, Reidel, New York, 1985, p. 457.
[15] K. Wada, K. Yoshida, T. Takatani, Y. Watanabe, Appl. Catal. A 99 (1993) 21.
[16] J. Cunningham, B.K. Hodnett, J. Chem. Soc., Faraday Trans. 1 77 (1981) 2777.
[17] A. Mattsson, M. Leideborg, K. Larsson, G. Westin, L. Österlund, J. Phys. Chem. B 110 (2006) 1210.
[18] K. Nakamoto, Infrared and Raman Spectra of Inorganic and Coordination Compounds, fifth ed., Wiley, New York, 1997.
[19] G. Busca, V. Lorenzelli, Mater. Chem. 7 (1982) 89.
[20] K.S. Kim, M.A. Barteau, J. Catal. 125 (1990) 353.
[21] L.-F. Liao, W.-C. Wu, C.-Y. Chen, J.-L. Lin, J. Phys. Chem. 105 (2001) 7678.
[22] D.S. Muggli, M.J. Backes, J. Catal. 209 (2002) 105.
[23] U. Diebold, Surf. Sci. Rep. 48 (2003) 53.
[24] B.E. Hayden, A. King, M.A. Newton, J. Phys. Chem. B 103 (1999) 203.
[25] H. Idriss, V.S. Lusvardi, M.A. Barteau, Surf. Sci. 348 (1996) 39.
[26] Y. Morikawa, I. Takahashi, M. Aizawa, Y. Namai, T. Sasaki, Y. Iwasawa, J. Phys. Chem. B 108 (2004) 14446.
[27] R.E. Tanner, Y. Liang, E.I. Altman, Surf. Sci. 506 (2002) 251.
[28] H. Uetsuka, M.A. Henderson, A. Sasahara, H. Onishi, J. Phys. Chem. B 108 (2004) 13706.
[29] F.P. Rotzinger, J.M. Kesselman-Truttman, S.J. Hug, V. Shklover, M. Grätzel, J. Phys. Chem. B 108 (2004) 5004.
[30] C.-C. Chuang, W.-C. Wu, M.-C. Huang, I.-C. Huang, J.-L. Lin, J. Catal. 185 (1999) 423.
[31] M. Andersson, L. Österlund, S. Ljungström, A. Palmqvist, J. Phys. Chem. B 106 (2002) 10674.
[32] M. Andersson, A. Kiselev, L. Österlund, A.E.C. Palmqvist, J. Phys. Chem. C 111 (2007) 6789.
[33] A. Kiselev, A. Mattsson, M. Andersson, A.E.C. Palmqvist, L. Österlund, J. Photochem. Photobiol. A 184 (2006) 125.
[34] S. Lundgren, K.-E. Keck, B. Kasemo, Rev. Sci. Instrum. 65 (1994) 2696.
[35] N. Serpone, A.V. Emeline, Int. J. Photoenergy 4 (2002) 91.
[36] H. Courbon, M. Formenti, F. Juillet, A.A. Lisachenko, J. Martin, S.J. Teichner, Kinet. Catal. 14 (1973) 84.
[37] M. Primet, P. Pichat, M.-V. Mathieu, J. Phys. Chem. 75 (1971) 1216.
[38] K. Tanaka, J.M. White, J. Phys. Chem. 86 (1982) 4708.
[39] G. Mul, A. Zwijnenburg, B. van der Linden, M. Makkee, J.A. Moulijn, J. Catal. 201 (2001) 128.
[40] G.B. Deacon, R.J. Phillips, Coord. Chem. Rev. 33 (1980) 227.
[41] M.A. Hasan, M.I. Zaki, L. Pasupulety, J. Phys. Chem. 106 (2002) 12747.
[42] M. El-Maazawi, A.N. Finken, A.B. Nair, V.H. Grassian, J. Catal. 191 (2000) 138.

[43] G.Y. Popova, T.V. Andrushkevich, Y.A. Chesalov, E.S. Stoyanov, Kinet. Catal. 41 (2000) 805.
[44] M.A. Henderson, J. Phys. Chem. B 108 (2004) 18932.
[45] J.M. Coronado, S. Kataoka, I. Tejedo-Tejedor, M.A. Anderson, J. Catal. 219 (2003) 219.
[46] J. Workman Jr., A. Springsteen, Applied Spectroscopy, Academic Press, London, 1998.
[47] G. Sokrates, Infrared Characteristic Group Frequencies, second ed., Wiley, Chichester, 1990.
[48] D. Brinkley, T. Engel, J. Phys. Chem. B 104 (2000) 9836.